SCIENCE CHINA
Technological Sciences

•Article•

October 2024 Vol.67 No.10: 3152–3167
https://doi.org/10.1007/s11431-023-2686-0

Thermal-hydraulic performance analysis and multi-objective optimization of a microchannel with staggered semi-elliptical ribs

CUI Pan, LIU Wei & LIU ZhiChun*

School of Energy and Power Engineering, Huazhong University of Science and Technology, Wuhan 430074, China

Received December 27, 2023; accepted May 22, 2024; published online September 13, 2024

To enhance the cooling capacity of traditional microchannels for high heat flux electronic devices, a microchannel design with staggered semi-elliptical ribs is proposed in this paper. Through numerical simulations, the flow characteristics of the designed microchannel are compared with those of a smooth one, and the effects of rib width (W_r), rib height (H_r), and rib length (L_r), on the thermal-hydraulic performance are investigated under laminar flow conditions. The results show that the periodically arranged ribs induce periodic vortices within the microchannel, effectively promoting fluid mixing and enhancing heat transfer. W_r and H_r have similar effects on microchannel performance, with an increase in them leading to an enhanced thermal performance at the expense of deteriorated hydraulic performance. Additionally, L_r has a comparatively weaker influence, with both the heat transfer and flow resistance initially growing with increasing L_r and then declining. To strike a balance between the two performances, a multi-objective optimization on the three geometrical parameters is conducted at a Reynolds number (Re) of 440. Combined with simulation data, artificial neural networks are trained as surrogate models, and a multi-objective genetic algorithm is employed to derive the Pareto front. Using the TOPSIS decision-making method, an optimal compromise solution is determined as W_r = 0.2415 mm, H_r = 0.0976 mm, and L_r = 0.6486 mm. Performance testing on the optimized microchannel reveals that it exhibits high heat transfer, middle flow resistance, and excellent overall performance, with the performance evaluation criterion (PEC) falling between 1.572 and 1.723 within the Re range of 220–660.

heat transfer enhancement, microchannel, semi-elliptical rib, numerical simulation, multi-objective optimization

Citation: Cui P, Liu W, Liu Z C. Thermal-hydraulic performance analysis and multi-objective optimization of a microchannel with staggered semi-elliptical ribs. Sci China Tech Sci, 2024, 67: 3152–3167, https://doi.org/10.1007/s11431-023-2686-0

1 Introduction

In recent years, electronic devices have been advancing towards high integration and miniaturization to meet the growing demand for improved performance and smaller size. Consequently, the heat flux generated within electronic devices has surged significantly. For instance, the heat dissipation requirement for traditional integrated circuits has reached 100 W cm^{-2}, while in very large-scale integration and advanced military equipment, it has exceeded 1000 W cm^{-2} [1,2]. High heat flux can lead to elevated operating temperature, which in turn, jeopardizes the stability and lifespan of electronic devices. According to statistical data, high temperature stands as the predominant cause of electronic device failures, accounting for approximately 55% of such failures [3]. To ensure the prolonged and stable operation of high power-density electronic devices, there is a critical need for efficient cooling technologies with small equipment size [4,5].

Microchannel cooling technology was initially introduced by Tuckerman and Pease [6], and it offers several advantages, including high heat transfer efficiency, large specific surface area, and compact dimensions. These qualities make it an effective solution for dissipating heat from high

*Corresponding author (email: zcliu@hust.edu.cn)

heat flux electronic devices [7]. However, for traditional microchannel heat sinks (MCHSs) with straight channels, the flow is predominantly in a laminar state, and the boundary layer continuously thickens along the mainstream direction, which deteriorates the cooling capacity. Therefore, extensive research has been conducted to improve the heat removal performance of microchannels. Contrasted with active heat transfer enhancement methods, passive methods are free of additional external components and often have high stability and robust in operation, thus garnering more attention [3]. Typical passive methods for channels include the use of additives in the fluid [8], alteration of the channel shape [9,10], surface treatment [11], and incorporation of spoilers such as ribs, fins, and cavities [12–14]. Of these, spoilers can increase the heat transfer area, introduce disturbances to the fluid, and serve as vortex generators to induce vortices that can promote the mixing of cold and hot fluids, making them an efficient and popular method.

Spoilers in microchannels are primarily incorporated with two designs: one arranged on the bottom of the microchannel, and the other arranged on the side walls. The ribs or fins on the bottom of the microchannel are usually situated near the central area, and they lead to enhanced heat transfer and high flow resistance [15]. In contrast, although spoilers on the sidewalls may not provide the same thermal performance due to the disturbances more closely to the walls, they offer better hydraulic performance. This configuration is particularly advantageous in specific laminar scenarios where strict constraints exist on power consumption and system volume. Chai et al. [16–18] comprehensively studied the thermal-hydraulic characteristics of laminar heat transfer in an MCHS with fan-shaped ribs on sidewalls. Compared with a smooth MCHS, they reported 6%–101% and 4%–103% increases in average Nusselt number for MCHS with aligned and offset fan-shaped ribs respectively, as well as the improved overall performance. Di Capua H et al. [19] numerically investigated the flow and heat transfer of microchannels with forward triangular ribs on sidewalls. They found the periodic break-up of boundary layer and vortices generated behind the ribs, leading to fluid mixing. As a result, the heat transfer and flow resistance increased simultaneously. Pan et al. [20] designed and fabricated an MCHS with fan-shaped cavities, and the experimental results revealed that it represented better heat transfer than a straight one. Khan et al. [21] designed an MCHS with rectangular ribs as turbulators, and the best turbulator arrangement exhibited the maximum Nusselt number of 21.8 within the studied flow conditions. The effects of rib geometry on the heat transfer and fluid flow of MCHS were numerically analyzed by Lori and Vafai [22]. The results showed that the rectangular and backward triangular ribs resulted in the highest pressure drop, while the elliptical ribs provided the highest thermal and overall performances. Wang et al. [23] and Lan et al. [15] designed MCHS with truncated ribs, and they found that compared with continuous ribs, truncated ribs could reduce flow resistance without heat transfer loss. Li et al. [24] designed an MCHS with dimples and pin-fins on sidewalls. The numerical results suggested enhanced heat transfer due to the optimized flow structures with symmetrical vortices.

However, it should be noted that ribs or fins located on the side walls with a height close to the channel will impose a great impact on the incoming flow, resulting in significant lateral velocity. Therefore, the induced vortices are typically local lateral vortices. In comparison to lateral vortices, longitudinal vortices extend along the mainstream direction and cover a larger region, suggesting the potential to achieve more efficient fluid mixing and thinning of the boundary layer [25]. Moreover, the increase in flow resistance caused by longitudinal vortices is less than that by lateral vortices [26,27]. Due to the superior performance, there is a growing number of research dedicated to developing new spoilers that can induce longitudinal vortices. Wang et al. [28] numerically studied the laminar heat transfer of a rectangular mini-channel with discrete double-inclined ribs on the bottom wall. Their results showed that the heat transfer was enhanced effectively by the double-inclined ribs which induced longitudinal vortices. Chen et al. [29] conducted experiments on microchannels with a few pairs of longitudinal vortex generators (LVGs), and they reported 12.3%–73.8% and 3.4%–45.4% increases in thermal performance of microchannels with aspect ratios of 0.0667 and 0.25, respectively. Ebrahimi et al. [30] and Zhang et al. [31] discussed the impacts of geometric parameters of LVG pairs on the flow and heat transfer characteristics of different configurations of microchannels. Gönül et al. [32] designed a microchannel with delta winglet-type vortex generators. They found that heat transfer enhancement primarily depended on the vortex structure, and the flow field with longitudinal vortices showed better thermal performance than that with transverse vortices. Cheng et al. [33] proposed an MCHS with LVGs and bypass jet flow, and the numerical results indicated that the induced longitudinal vortices contributed to the drastic mixing of the coolant fluid. Zheng et al. [34] explored the thermal–hydraulic characteristics of a mini-channel with trapezoidal cross-section LVGs on the bottom wall, and they found it exhibited better overall performance than rectangular LVGs. Feng et al. [35] conducted experimental and numerical investigations on mini-channels with the insertion-type LVGs. Their results indicated the generation of vortex flow and favorable overall performance. Overall, longitudinal vortices can enhance the thermal performance of microchannels while usually maintaining good overall performance. However, existing spoilers capable of inducing longitudinal vortices are mostly arranged on the bottom wall. As mentioned earlier, this design may lead to relatively

higher flow resistance.

Recently, Feng et al. [36] reported a microchannel with staggered triangular ribs arranged on both the bottom and top surfaces. The numerical results demonstrated the generation of vortex flow, enhanced heat transfer, and reasonable flow resistance. The maximum performance evaluation criterion (PEC) of 1.502 was achieved occurring at a Reynolds number of 639. However, there were regions with very low velocity behind the right-angled ribs, which deteriorated the heat transfer to a certain extent. Al-Asadi et al. [37] compared the heat transfer of microchannels with quarter and half cylindrical ribs on the bottom wall. They found that in most cases, the quarter cylindrical ribs did not effectively reduce the thermal resistance, primarily due to the presence of large low-velocity regions behind them. On the contrary, microchannels with half-cylindrical ribs exhibited greatly enhanced heat transfer. This suggests that ribs with expanding-constricting cross sections may provide better performance for microchannels than those with solely expanding cross sections, as they can reduce low-velocity regions. It is consistent with the results of Lori and Vafai [22].

In addition to designing enhanced structures, parameter optimization is another effective approach to further improve microchannels' performance. Compared to selecting a solution from limited samples, the use of optimization algorithms allows for the exploration of the upper limit of performance to achieve greater improvement. Among them, intelligent optimization algorithms, such as the genetic algorithm (GA), stand out for the advantages of global search capability, high efficiency, and wide applicability, which have been extensively adopted in the optimization of convective heat transfer [38–41]. Another crucial aspect of optimization design is the forward problem-solving scheme, which involves obtaining the output physical performance based on input parameters. Unlike computational fluid dynamics (CFD) requiring iterative calculations, constructing a surrogate model based on a certain number of samples to fit the input and output can significantly improve efficiency while maintaining an acceptable level of accuracy. Therefore, combining surrogate models with intelligent optimization algorithms is an efficient and accurate method to perform optimization design. Yang et al. [42] presented a parameter optimization on two types (A type and B type) of MCHS with response surface methodology (RSM) and GA. Compared with the original designs, the heat transfer of the optimal designs for the A-type and B-type were increased by 12.67% and 8.31%, respectively. Husain and Kim [43] conducted an optimization design on an MCHS with thermal resistance and pumping power as objective functions. The Pareto front was obtained by the non-dominated sorting genetic algorithm II (NSGA-II) coupled with surrogate models. Artificial neural networks and NSGA-II were employed by Sikirica et al. [44] to optimize microchannels with secondary channels and with ribs. The trained surrogate model was demonstrated to make accurate predictions. The obtained designs could attain temperatures lower by more than 10% compared to original designs under the same pressure limit, or pressure drops reduced by more than 25% when limited by temperature. Das and Hiremath [45] carried out a multi-objective optimization on a butterfly-wing vortex generator to balance the trade-off between the increment of heat transfer and the decrement of flow resistance and total entropy-generation. Wang et al. [46] implemented a numerical and experimental optimization on a bidirectional-ribbed microchannel. The selected optimal compromise solution by the Technique for Order Preference by Similarity to Ideal Solution (TOPSIS) decision-making method showed good overall performance.

Based on the literature review, a microchannel design with staggered semi-elliptical ribs is proposed in this paper to induce longitudinal vortices for high heat transfer without significantly increasing flow resistance. The ribs are designed with an expanding-constricting cross section to reduce low-velocity regions. Numerical simulations are conducted to analyze the flow characteristics within the ribbed microchannel. The effects of rib width, rib height, and rib length on the thermal and hydraulic performances of the microchannel are explored. Subsequently, artificial neural networks are combined with GAs to conduct a multi-objective optimization on the three geometric parameters. Finally, the TOPSIS method is employed to determine an optimal compromise solution from the Pareto front, striking a balance between thermal and hydraulic performances.

2 Numerical simulation

2.1 Physical model

The microchannel with semi-elliptical ribs is depicted in Figure 1, where two columns of ribs are arranged diagonally in the cross-sectional direction. Given the symmetry of MCHS, only a single microchannel with symmetry boundary condition is considered, which is a commonly employed simplification in the numerical simulation of MCHS. The computational model consists of both the fluid and solid domains, with the latter incorporating the ribs. The glass cover at the top of the microchannel is neglected. To prevent backflow at the microchannel outlet, the fluid domain is extended by 5 mm, which is over 10 times of its characteristic length. As shown in Figure 1(b) and (c), the length L, width W, and height H of the solid domain are 20, 0.6, and 0.6 mm, respectively. The width W_{ch} and height H_{ch} of the fluid domain are both 0.4 mm. The distance between adjacent ribs in the same column is 1 mm. The design parameters of the ribs include the rib width W_r, rib height H_r, and

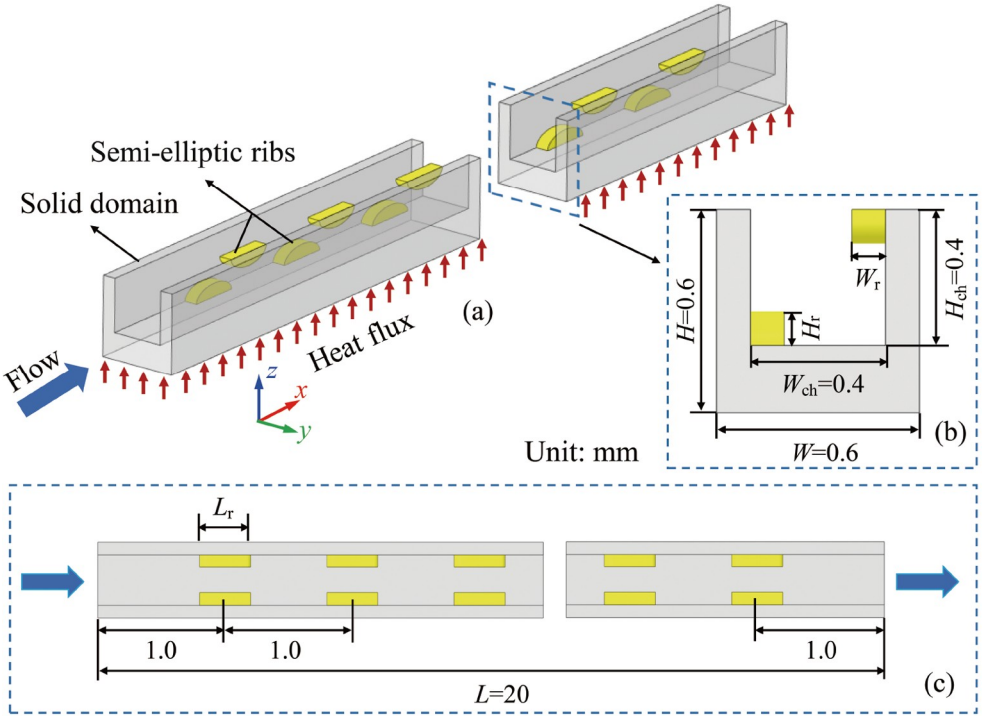

Figure 1 Schematic diagrams and dimensions of the designed microchannel. (a) Physical model; (b) cross-sectional view; (c) top view.

rib length L_r, with the investigated values presented in Table 1.

2.2 Numerical method and boundary conditions

In this study, several assumptions are made to simplify the numerical simulation. The coolant water is treated as a continuous, incompressible Newtonian fluid. The flow is assumed to be single-phase, steady, and laminar. Viscous dissipation, radiation, and gravity effect are neglected. Based on the assumptions, the governing equations are formulated as follows.

Continuity equation:

$$\nabla \cdot (\rho \mathbf{U}) = 0. \tag{1}$$

Momentum equation:

$$\nabla \cdot (\rho \mathbf{U}\mathbf{U}) = -\nabla p + \nabla \cdot (\mu(\nabla \mathbf{U} + \nabla \mathbf{U}^{\mathrm{T}})). \tag{2}$$

Energy equation for fluid domain:

$$\nabla \cdot (\rho c_{\mathrm{p}} \mathbf{U} T) = \nabla \cdot (\lambda_{\mathrm{f}} \nabla T). \tag{3}$$

Energy equation for solid domain:

$$\nabla \cdot (\lambda_{\mathrm{s}} \nabla T) = 0, \tag{4}$$

where $\mathbf{U}$ represents velocity vector, p denotes pressure, and T is temperature. The dynamic viscosity μ is represented by a piecewise linear function of temperature, with breakpoints provided in Table 2 [47]. The relationships for the density ρ, thermal conductivity λ_{f}, and specific heat capacity c_{p} of water as functions of temperature are given by eqs. (5)–(7) [15], respectively. In eq. (5), T is in °C, while in eqs. (6) and (7), it is in K. The thermal conductivity λ_{s} of the solid material, silicon, is a constant value of 148 W m^{-1} K^{-1}.

$$\begin{aligned}\rho = {} & (998.84 + 18.225T - 7.92 \times 10^{-3}T^2 \\ & - 5.545 \times 10^{-5}T^3 + 1.498 \times 10^{-7}T^4 \\ & - 3.933 \times 10^{-10}T^5) / (1 + 1.816 \times 10^{-2}T),\end{aligned} \tag{5}$$

$$c_{\mathrm{p}} = 8958.9 - 40.535T + 0.11243T^2 - 1.014 \times 10^{-4}T^3, \tag{6}$$

$$\lambda_{\mathrm{f}} = -0.58166 + 6.3556 \times 10^{-3}T - 7.964 \times 10^{-6}T^2. \tag{7}$$

The boundary conditions are set as follows. At the inlet of the fluid domain, uniform velocity and temperature distributions are imposed, and the inlet temperature is 293.15 K. The outlet of the fluid domain is set as a pressure outlet with a gauge pressure of 0 Pa. Symmetric boundary conditions are applied to the two sides of the solid domain. At the bottom of the solid domain, a uniform heat flux of q = 100 W cm^{-2} is adopted. No-slip and coupled boundary conditions are utilized at the fluid-solid interfaces. The top surface of the fluid domain and the surfaces of the fluid extension section are

Table 1 Investigated parameter values of the ribs

Parameter	Value (mm)
W_{r}	0.05, 0.10, 0.15, 0.20, 0.25, 0.30
H_{r}	0.03, 0.6, 0.9, 0.12, 0.15, 0.18
L_{r}	0.3, 0.4, 0.5, 0.6, 0.7

Table 2 The relationship between the dynamic viscosity and temperature of water

T (K)	μ (kg m^{-1} s^{-1})	T (K)	μ (kg m^{-1} s^{-1})	T (K)	μ (kg m^{-1} s^{-1})	T (K)	μ (kg m^{-1} s^{-1})
293.15	1.0016×10^{-3}	313.15	6.527×10^{-4}	333.15	4.660×10^{-4}	353.15	3.541×10^{-4}
303.15	7.972×10^{-4}	323.15	5.465×10^{-4}	343.15	4.036×10^{-4}	363.15	3.142×10^{-4}

assigned no-slip and adiabatic boundary conditions, while the remaining solid surfaces are considered adiabatic.

Numerical simulations are performed on the ANSYS Fluent 19.0 platform. The governing equations are discretized with the second-order upwind scheme, and the pressure-velocity coupling is implemented using the Coupled algorithm. The solution is considered converged when the residuals for the continuity equation, momentum equation, and energy equations are below 10^{-5}, 10^{-6}, and 10^{-8}, respectively.

2.3 Data reduction

The hydraulic diameter D_h of the microchannel is defined as

$$D_h = \frac{2W_{ch}H_{ch}}{W_{ch}+H_{ch}}. \tag{8}$$

The definition of the Reynolds number (Re) is as follows:

$$Re = \frac{\rho_{in}u_{in}D_h}{\mu_{in}}, \tag{9}$$

where the subscript "in" represents the inlet. The fanning friction factor (f) is employed to characterize the hydraulic performance of the microchannel, which is expressed as

$$f = \frac{\Delta pD_h}{2\rho_m u_{in}^2 L}, \tag{10}$$

where Δp is the pressure drop between the inlet and outlet of the microchannel, and the subscript "m" denotes that this physical quantity is based on the arithmetic mean temperature at the inlet and outlet of the microchannel. The Nusselt number (Nu) is used to characterize the thermal performance and defined as

$$Nu = \frac{hD_h}{\lambda_{fm}}. \tag{11}$$

The convective heat transfer coefficient (h) is given by

$$h = \frac{qLW}{A_{f\text{-}s}(T_w - T_m)}, \tag{12}$$

where $A_{f\text{-}s}$ is the heat transfer area of the interface between the fluid and solid and is variable with the parameters of the ribs. T_w is the average temperature of the heated wall, and T_m represents the arithmetic mean temperature at the inlet and outlet of microchannel. Ribs can enhance heat transfer but also lead to an increase in flow resistance, so the PEC is used to assess the overall performance of the microchannel:

$$\mathrm{PEC} = \frac{Nu/Nu_0}{(f/f_0)^{1/3}}, \tag{13}$$

where the subscript "0" denotes the smooth microchannel.

2.4 Validations of grid independence and numerical method

The computational domain discretization and mesh generation are performed using the Fluent Meshing 19.0 software. Hexahedral grids are adopted in the central regions of both the fluid and solid domains, and boundary layers are added to capture local hydraulic and thermal characteristics. Polyhedral grids are filled between the boundary and central regions, which can reduce the grid number while maintaining computational accuracy. The test condition is set as W_r = 0.15 mm, H_r = 0.15 mm, L_r = 0.5 mm at Re = 440. Using the same grid generation method, four mesh sets are created with grid numbers of 1334702, 2817672, 4936959, and 8659267, respectively. The obtained Nu and f from each mesh system are presented in Figure 2. Compared with the results of the mesh system containing 8659267 grids, it is found that when the grid number reaches 4936959, the relative errors of Nu and f are 0.59% and 0.92%, respectively. This suggests that the effect of further increasing grid number on the simulation results is negligible. Considering both computational accuracy and efficiency, the mesh system with 4936959 grids is chosen for subsequent simulations.

To verify the adopted numerical method, the simulation results of an MCHS with fan-shaped reentrant cavities are compared with the experimental results by Chai et al. [48]. The microchannel examined in their study featured a hydraulic diameter of 0.133 mm and a length of 10 mm. The cavity had a field angle of 120° with a radius of 0.1 mm. Silicon was employed as the solid material, and distilled water served as the working fluid. The inlet temperature was

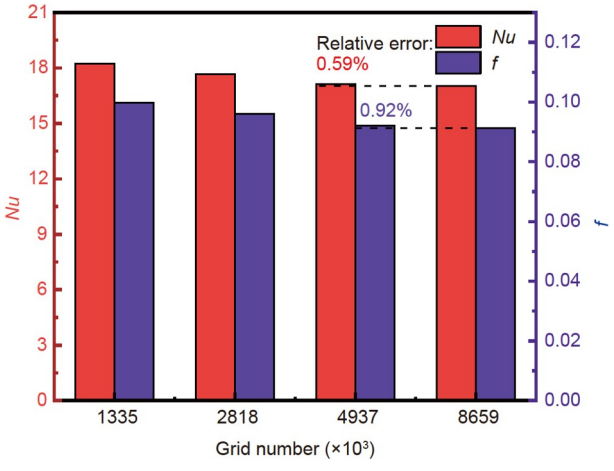

Figure 2 Validation of grid independence.

set to 293 K, and the heat flux was 0.6 MW m^{-2}. With the same physical model and operating conditions, Figure 3 displays the comparison between the simulation results obtained using the described numerical method and the experimental results by Chai et al. In this figure, *Nu* and $f_{app}Re$ represent the thermal and hydraulic performances of the MCHS respectively. Overall, the simulation results closely agree with the experimental data. When *Re* is less than 700, both the *Nu* and $f_{app}Re$ from numerical simulations fall within the margin of experimental error. For the cases of *Re* exceeding 700, the errors slightly increase, but the maximum relative errors remain below 10%. These test results demonstrate the reliability of the numerical method employed in this paper, where *Re* is in the range of 220–660.

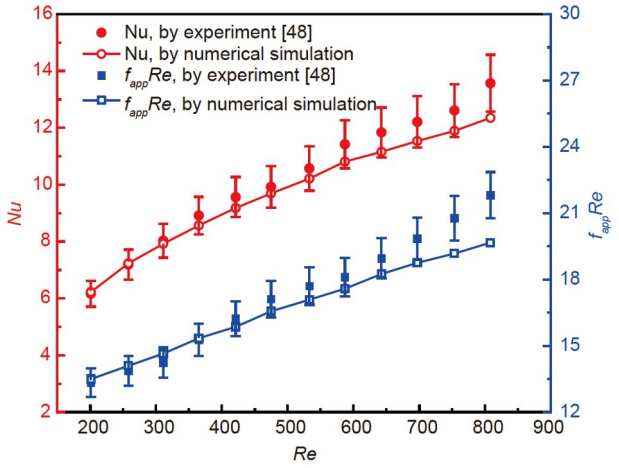

Figure 3 Verification of present numerical results with experimental results by Chai et al. [48].

3 Results and discussion

3.1 Comparison of flow field characteristics

The influence of semi-elliptical ribs on the flow field of the microchannel is analyzed initially. Figure 4 presents a comparison of velocity and streamline contours at different cross sections within a single channel unit for both the smooth and designed microchannels at *Re* = 440. In this case, W_r, H_r, and L_r are taken as 0.2, 0.15, and 0.5, respectively. Since variations in the flow field of the smooth microchannel are relatively small, only the contours at two cross sections, namely *x* = 10.5 mm and *x* = 11.1 mm, are displayed. It can be observed that the flow in the smooth microchannel develops a thick boundary layer due to the absence of disturbance, especially in the corners of the channel. However, in the microchannel with semi-elliptical ribs, the ribs generate disturbances to the fluid and induce longitudinal vortices of varying sizes within the channel. As the flow approaches the ribs, these vortices gradually form and extend from near the walls towards the central area of the channel. The low-velocity regions at the corners of the channel gradually diminish as well. When the fluid flows over the ribs, the reduction in flow area leads to an increase in local velocity, thus intensifying the local jet effect. In this scenario, there is essentially no low-velocity region, and the induced two pairs of vortices mostly disappear. Nevertheless, once the fluid gradually passes over the ribs, the adverse pressure gradient causes boundary layer separation, accompanied by the generated tangential velocity, resulting in the formation of new vortices and low-velocity regions. Consequently, the periodically arranged ribs induce periodic vortices and low-velocity regions. The rear sections of semi-elliptical ribs serve as a flow-diverting structure and occupy a portion of

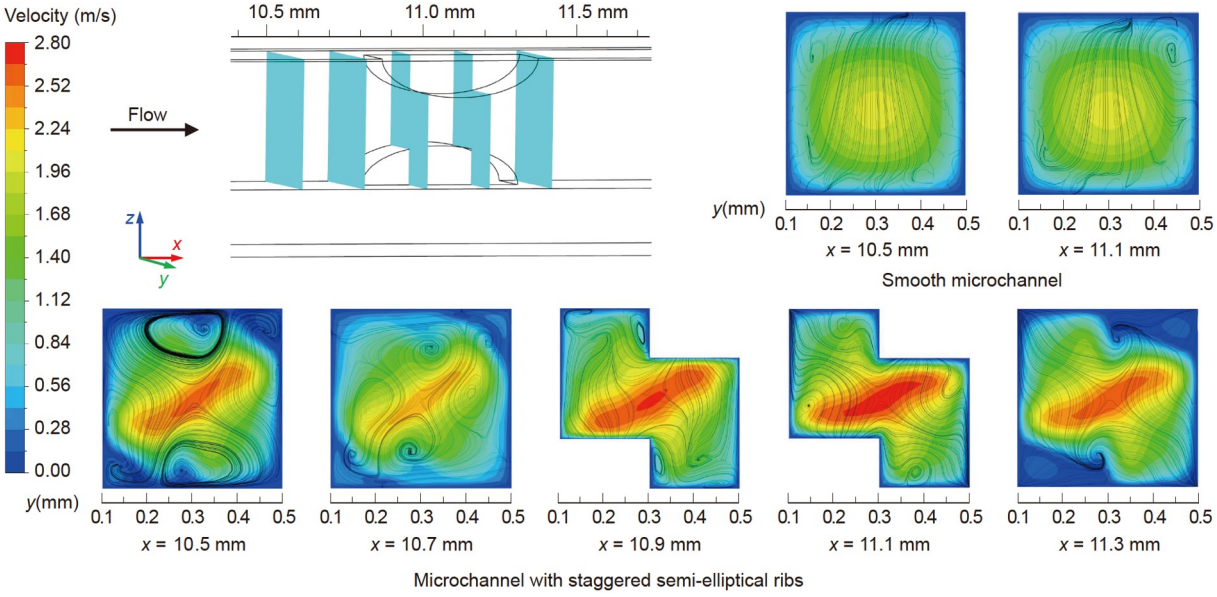

Figure 4 Comparison of the velocity and streamlines contours at different cross sections between the smooth and designed microchannels at *Re* = 440.

space, which is conducive to reducing low-velocity regions. Compared to the smooth microchannel, the introduction of semi-elliptical ribs significantly reduces the thickness of the boundary layer. On one hand, the increase in local velocity contributes to a thinner boundary layer, while on the other hand, the ribs periodically disrupt the development of the boundary layer.

3.2 The effect of rib width

Figure 5 illustrates the distributions of velocity, streamlines, and temperature at the cross section of x = 10.7 mm for different rib widths W_r at Re = 440, while keeping H_r = 0.15 mm and L_r = 0.5 mm. In Figure 5(a), when W_r is small, the influence of ribs on the flow field is limited, and vortex flow is not significant. As W_r increases, the vortices become more prominent, and the vortex regions gradually expand. When W_r reaches 0.20 mm, the vortex flow almost affects the entire flow field at the cross section. Since the ribs are arranged diagonally, the vortices are also distributed diagonally, while their locations shift with the change of W_r. A larger W_r enhances the jet effect, creating a greater disturbance, which results in the continuous thinning of the boundary layer and faster disappearance of the low-velocity regions. Comparing Figure 5(a) and (b), it is evident that the temperature distribution is consistent with the velocity distribution, indicating the influence of the velocity field on the temperature field. In the straight channel region without ribs, the vortices can entrain the hot fluid from the lower part of the microchannel and the cold fluid from the upper part into the central region, promoting the mixing of hot and cold fluids and improving temperature uniformity. In the ribbed regions, the ribs on the bottom and top surfaces of the microchannel induce positive and negative z-velocity to the fluid respectively, which also improves fluid mixing. Consequently, the temperature uniformity of the fluid is improved significantly due to the larger vortices and entrainment caused by the increased W_r. When W_r reaches 0.2 mm, there are no large regions of low temperature in the center of the microchannel. The strong disturbance and jet effect also lead to a thinning of the thermal boundary layer. The addition of ribs in the microchannel has a minimal impact on the area of the fluid-solid interface but greatly enhances heat transfer due to the introduced disturbances and vortices.

To quantitatively analyze the influence of W_r on the thermal-hydraulic performance of the microchannel, the variations of Nu and f with W_r at different Re numbers are plotted in Figure 6. As shown in Figure 6(a), Nu increases with the increase of W_r within the Re range of 220–660. This enhancement can be attributed to the fact that larger W_r enlarges the vortex flow regions and local jet effect, leading to a thinner thermal boundary layer and improved temperature uniformity. Consequently, the thermal performance of the microchannel is enhanced. It is noted that the growth rate of Nu gradually decreases, especially when W_r exceeds 0.25 mm. This is primarily due to the expansion of low velocity regions behind the ribs, which weakens heat transfer to some extent. Furthermore, the thermal performance of the microchannel improves with the increasing Re, which provides larger velocity and a thinner thermal boundary layer. For W_r ranging from 0.05 to 0.30 mm and Re within the range of 220–660, Nu falls in the range of 6.04–21.99.

Regarding the hydraulic performance, as depicted in Figure 6(b), f gradually increases with the increment of W_r, and the growth rate becomes larger. This can be attributed to the

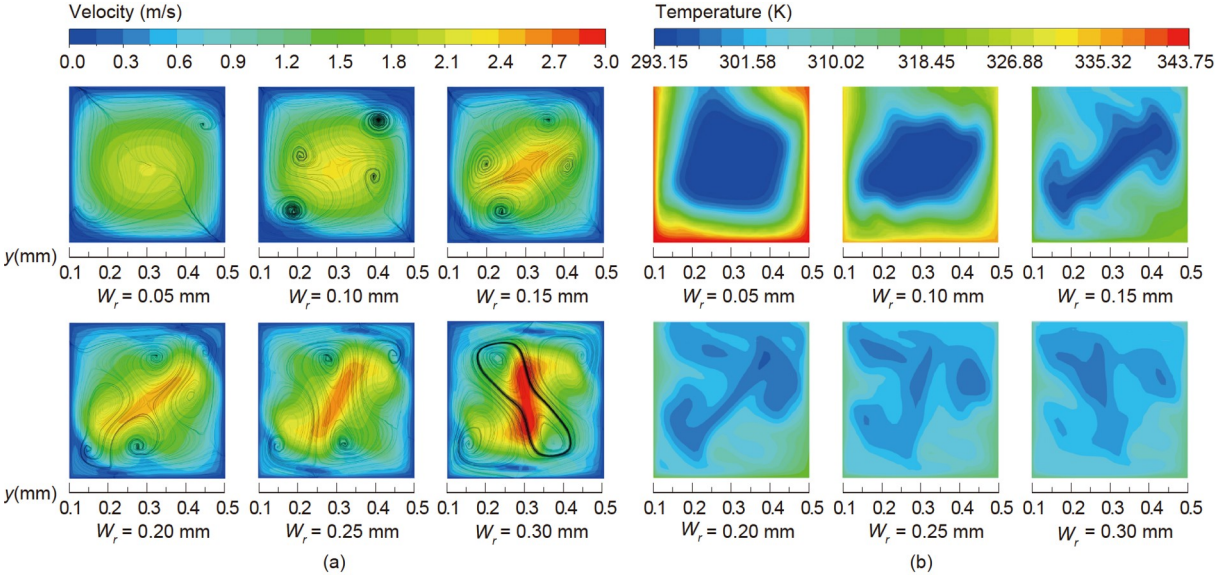

Figure 5 Contours of velocity, streamlines, and temperature at the microchannel cross section of x = 10.7 mm for different W_r at Re = 440.

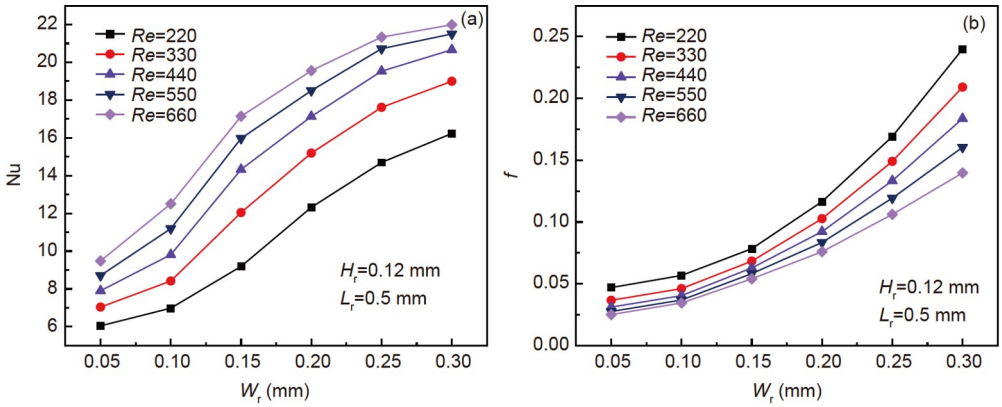

Figure 6 (Color online) Variations of (a) *Nu* and (b) *f* with W_r at different *Re* numbers.

higher local velocity resulting in larger viscous stress, and expanded vortex regions rendering greater loss of mechanical energy. By comparing Figure 6(a) and (b), it is evident that when W_r becomes excessively large, the growth rate of *Nu* is significantly smaller than that of *f*, which means the loss of pump power outweighs the gain of heat transfer. For W_r ranging from 0.05 to 0.30 mm and *Re* within the range of 220–660, *f* falls in the range of 0.025–0.240.

Figure 7 depicts the relationship between the PEC and W_r at different *Re* numbers. As W_r gradually increases from a small value, both *Nu* and *f* increase, but the increase in heat transfer outweighs flow resistance, resulting in higher PEC values. However, when W_r exceeds a critical value, further increasing in W_r lead to diminishing returns in heat transfer compared to flow resistance. This transition is characterized by a gradual decrease in PEC, although it remains greater than 1. The PEC exhibits this increasing-decreasing trend with W_r for different *Re* numbers, but the critical transition values of W_r vary with *Re*. In the cases of high *Re* numbers, this transition occurs at smaller W_r values. This is because larger *Re* values provide higher velocity and thinner boundary layer, so a small W_r is required for further enhancement without significant increase in flow resistance. Therefore, to achieve high overall performance, a large W_r is preferable for low *Re* conditions, while a small W_r is desirable for high *Re* conditions. Notably, the maximum PEC value in Figure 8 is observed at W_r = 0.25 mm and *Re* = 330, with a specific value of 1.619.

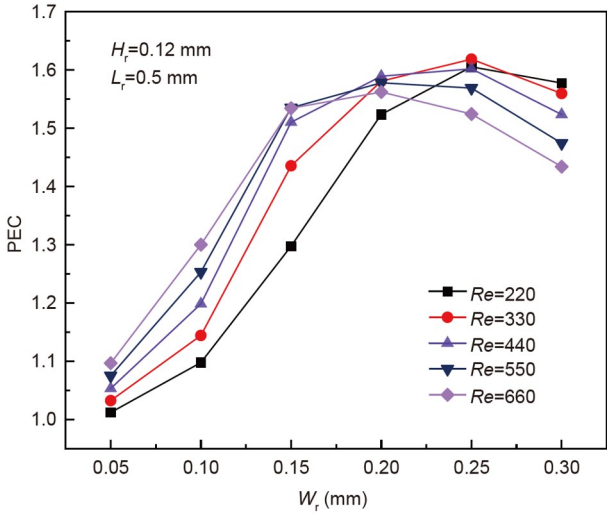

Figure 7 (Color online) Variations of PEC with W_r at different *Re* numbers.

3.3 The effect of rib height

Keeping W_r = 0.20 mm and L_r = 0.5 mm, the influence of rib height H_r on the thermal and hydraulic characteristics of the microchannel is analyzed. Figure 8 displays the distributions of velocity, streamlines, and temperature at the cross section of *x* = 10.7 mm for different H_r values at *Re* = 440. In Figure 8(a), it can be seen that the ribs of different heights induce vortices within the microchannel. As H_r increases, the characteristics of vortices initially become more pronounced while then diminishing, as evidenced by the spiral and curved streamlines. This decline can be attributed to that when H_r is too large, flow separation leads to a significant expansion of low velocity regions in the height direction. However, the length of straight channel within one unit to dissipate the low velocity regions remains unchanged. As a result, the development of vortices is constrained by the low velocity regions. Nevertheless, larger H_r values still induce substantial vortex sizes, stronger disturbances, and prominent jet effect. As demonstrated in Figure 8(b), the thermal boundary layer gradually thins, and the temperature uniformity of the fluid improves with increasing H_r, resulting in enhanced heat transfer. When H_r reaches 0.12 mm, the temperature distribution has been significantly improved while showing smaller changes as H_r further increases.

The variations of *Nu* and *f* with H_r at different *Re* numbers are illustrated in Figure 9. From Figure 9(a), it can be observed that *Nu* increases with increasing H_r and *Re*. This is

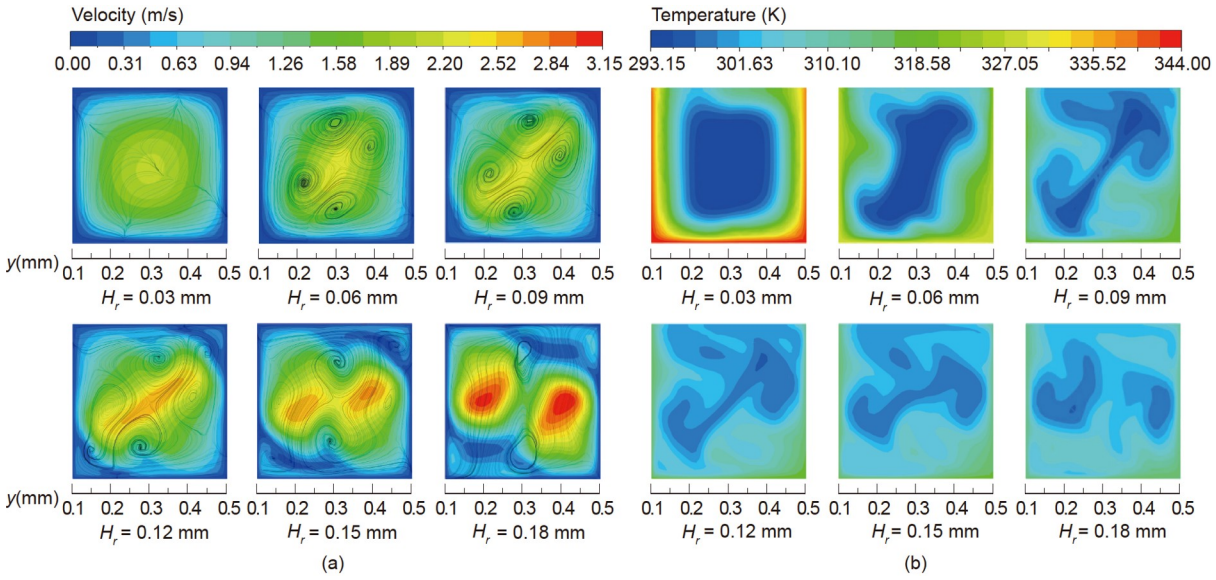

Figure 8 Contours of velocity, streamlines, and temperature at the microchannel cross section of x = 10.7 mm for different H_r at Re = 440.

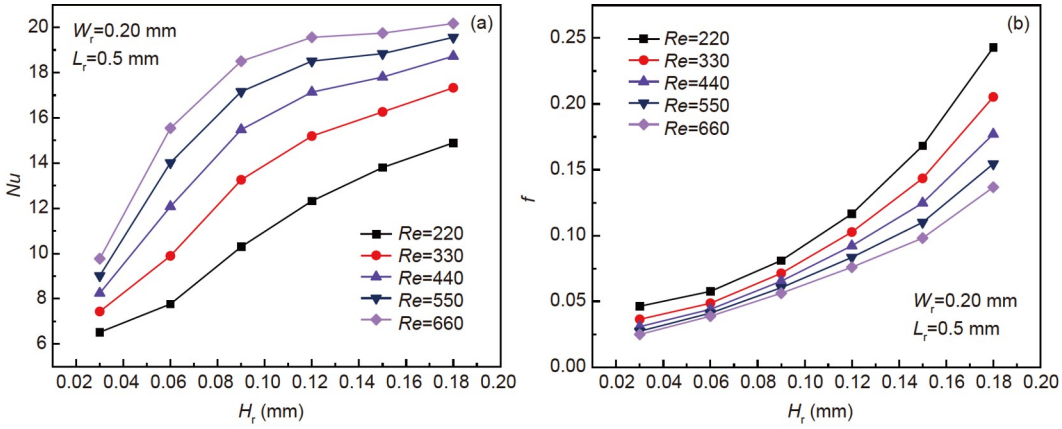

Figure 9 Variations of (a) Nu and (b) f with H_r at different Re numbers.

primarily attributed to stronger disturbances and higher velocity. However, the rate of increase in Nu with H_r gradually diminishes, particularly at Re = 660, where the growth in Nu becomes minimal after H_r reaches 0.12 mm, and it is less than that shown in Figure 6(a). The reason behind this is that larger H_r leads to extended low velocity regions, resulting in weakened fluid mixing and less pronounced vortices. Similar to the effect of W_r, increasing H_r leads to an increase in f, and the growth rate becomes larger. This is also due to the increased viscous stress and mechanical energy loss. Overall, for H_r ranging from 0.03 to 0.18 mm and Re within the range of 220–660, Nu and f of the microchannel fall in the ranges of 6.52–20.16 and 0.025–0.243, respectively.

The variations of PEC with H_r at different Re numbers is presented in Figure 10. As H_r increases, PEC shows an increase-decrease trend. When H_r is below a certain critical value, the enhancement in Nu is greater than that in f, resulting in an increase in PEC. However, as H_r surpasses this critical value, further increase in H_r leads to a situation where the enhancement in heat transfer becomes relatively weaker compared to the increase in flow resistance. This results in a gradual decrease in PEC. Similarly, for lower Re conditions, a larger H_r is preferable to achieve high PEC values, whereas the opposite holds true for higher Re conditions. The maximum PEC value in Figure 11 is observed at H_r = 0.09 mm and Re = 660, with a specific value of 1.635.

3.4 The effect of rib length

Figure 11 provides the distributions of velocity, streamlines, and temperature at two segments of longitudinal sections for different rib lengths L_r at Re = 440. The two sections are positioned at y = 0.2 mm and y = 0.4 mm, respectively. As shown in the previous contours, the y coordinate of the microchannel ranges from 0.1 to 0.5 mm, so the two sections pass through the centers of two ribs within one channel unit.

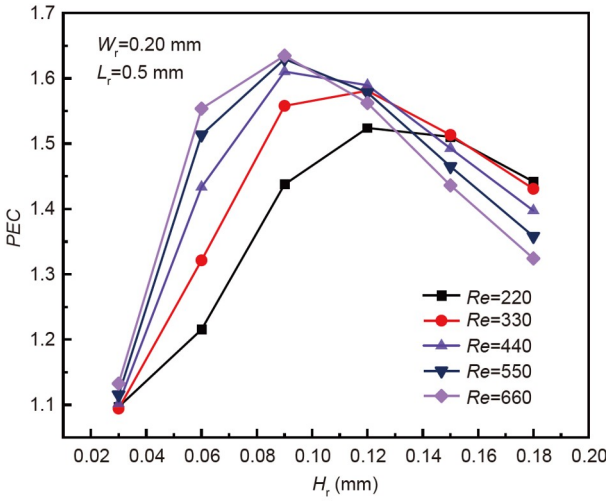

Figure 10 Variations of PEC with H_r at different *Re* numbers.

In the *x* direction, they span from 10.5 to 11.5 mm. It can be observed that when L_r is small, the ribs' curvature is large, resulting in an effect similar to that of a large H_r. This leads to significant low-velocity regions behind ribs, and the development of vortices is constrained. It is noted that low-velocity regions are also observed in front of the ribs, which originate from the previous channel unit and have not completely disappeared yet. With a gradual increase in L_r, the low-velocity regions initially contract and then expand, while vortices become more significant and then diminish correspondingly. The reduction in low-velocity regions is related to the change in the position of flow separation and the drainage of the rear section of the ribs. The subsequent increase is attributed to the decrease in the length of the straight channel within a single unit for dissipating the low-velocity regions. The temperature distribution presented in Figure 11(b) correlates with the velocity distribution. When L_r is small, the distinct high and low-velocity regions result in temperature stratification. Moreover, noticeable regions with high temperatures are observed behind the ribs, as marked in Figure 11(b). As L_r increases, the fluid mixing is strengthened, leading to improved temperature uniformity and weakened temperature stratification. However, excessively large L_r exacerbates the expansion of low-velocity regions, deteriorating fluid mixing and reducing temperature uniformity once again. The optimal temperature distribution for heat transfer depicted in Figure 11(b) is achieved at L_r = 0.5 or 0.6 mm.

The variations of *Nu*, *f*, and PEC with L_r at different *Re* numbers are presented in Figure 12. It is found that all three physical quantities initially increase and then decrease with the increase of L_r. This trend is related to the changes in vortex flow, low velocity regions, and temperature uniformity within the microchannel. The microchannels with L_r = 0.5 and 0.6 mm exhibit higher thermal performance, which is consistent with the better temperature uniformity and thinner thermal boundary layer shown in Figure 11(b). In comparison to W_r and H_r, the influence of L_r on the microchannel performance is relatively weaker, specifically on hydraulic performance. It is because when L_r is small, although the low velocity regions are large, they limit the development of vortices and subsequent mechanical energy loss. When L_r is large, the increase in local velocity is not significant as that of W_r and H_r, and the vortices are still limited by the short straight channel. Therefore, the energy loss caused by L_r is not as large as that by W_r and H_r. Furthermore, as *Re* increases, the corresponding L_r for the transition points where *Nu* and *f* change from increasing to

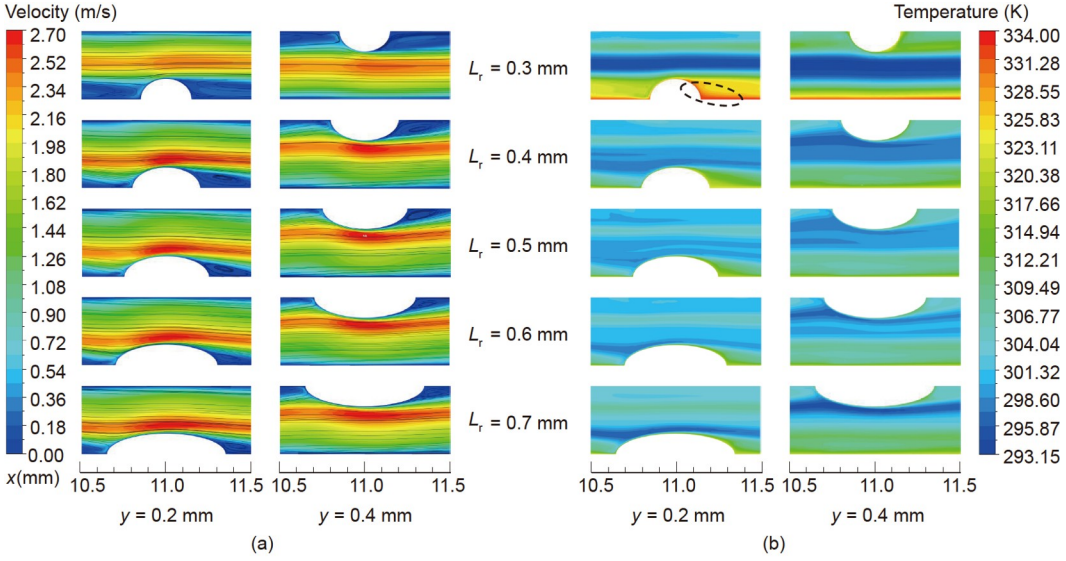

Figure 11 Contours of velocity, streamlines, and temperature at the segmented longitudinal sections of y = 0.2 mm and y = 0.4 mm for different L_r at *Re* = 440.

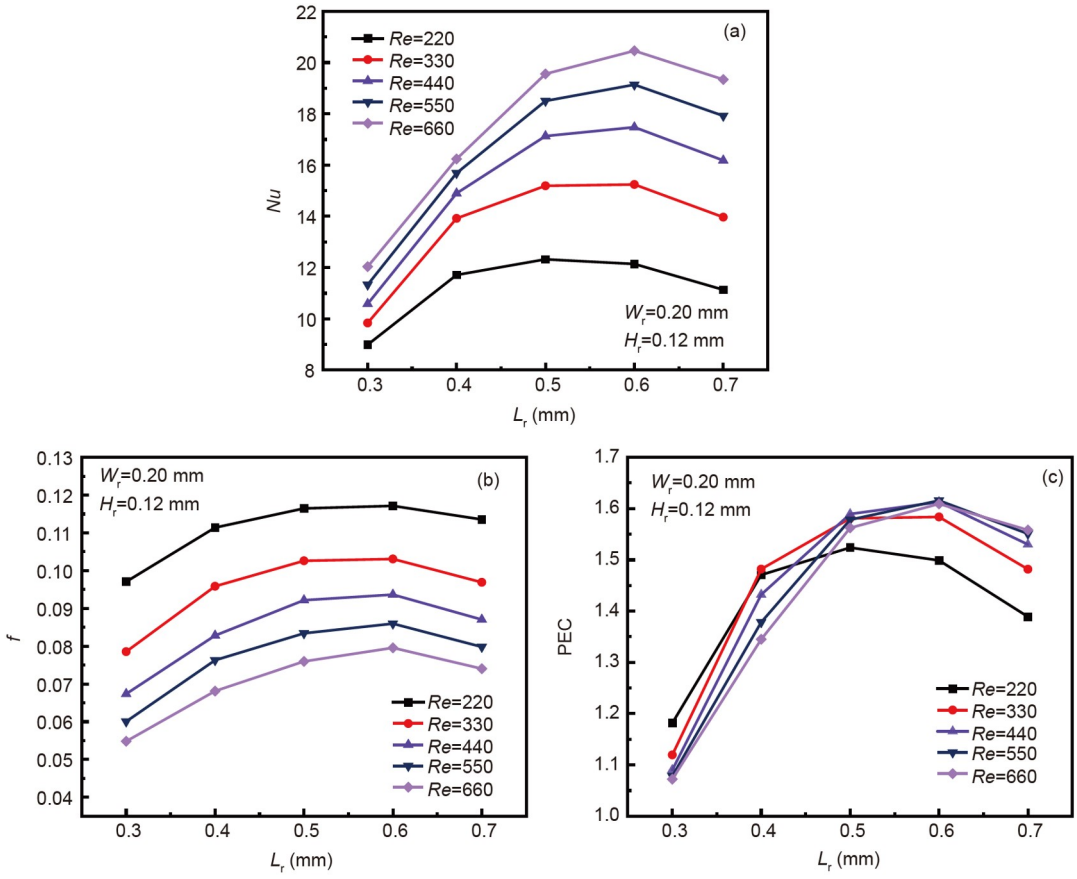

Figure 12 (Color online) Variations of (a) *Nu*, (b) *f*, and (c) PEC with L_r at different *Re* numbers.

decreasing becomes larger. This is because high flow velocity can reduce low velocity regions, and weak local disturbances caused by large L_r has a more pronounced enhancement effect compared to situations where the low velocity regions are larger. Comparing Figure 12(a) and (b), it can be seen that increasing L_r within a certain range (0.4–0.6 mm) is capable of improving thermal performance without significantly deteriorating hydraulic performance, which is conducive to achieving high overall performance. In general, the influence of L_r on the thermal and hydraulic performances of the microchannel is weaker than that of W_r and H_r, while they show similar impacts on the overall performance. The maximum PEC value in Figure 12(c) is observed at L_r = 0.6 mm and *Re* = 550, with a specific value of 1.641.

3.5 Comparison with previous works

According to the numerical results, the microchannel design proposed in the present work exhibits excellent overall performance. To provide a more intuitive representation of its performance, the PEC of the microchannel with W_r = 0.20 mm, H_r = 0.12 mm, and L_r = 0.5 mm is compared to that of several previously reported microchannel designs. This comparison is illustrated in Figure 13, where examples include microchannels with fan-shaped ribs by Chai et al. [18], truncated fins by Lan et al. [15], staggered triangular ribs by Feng et al. [36], offset forward triangular fins by Chai et al. [49], half cylindrical ribs on the bottom wall by Al-Asadi et al. [37], semicircular grooves by Zhu et al. [50], and butterfly insert by Sudheer and Madanan [51] capable of introducing vortices. As shown in Figure 13, the PEC values of different microchannels exhibit varying trends with *Re*. Microchannels with truncated fins [15], staggered triangular ribs [36], and butterfly insert [51] exhibit a pronounced increase in PEC with increasing *Re*, while microchannels with fan-shaped ribs [18] and offset forward triangular fins [49] initially experience an increase in PEC followed by a continuous decrease as *Re* increases. Additionally, there are microchannels, as observed in refs. [37] and [50], whose PEC is relatively less affected by *Re*. In comparison to these microchannels, the proposed microchannel consistently maintains the highest PEC values within the *Re* range of 220–660. Furthermore, the PEC exhibits minimal variations with *Re*, remaining at a high level. In summary, the proposed microchannel design can maintain high overall performance over a relatively wider range of *Re*, rendering it suitable for more flow conditions.

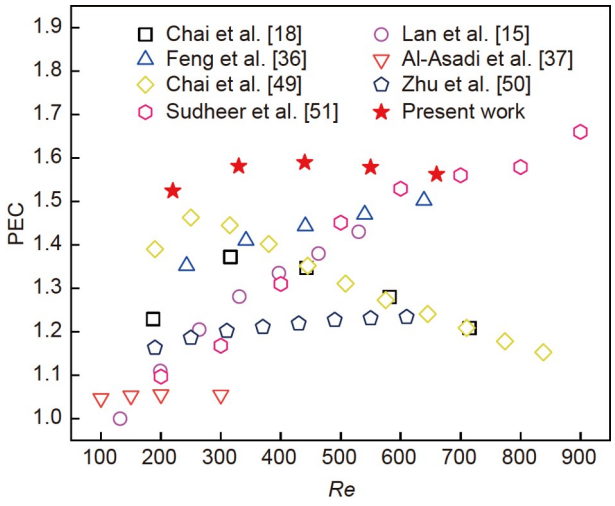

Figure 13 (Color online) Comparison of PEC with previous works.

4 Multi-objective optimization

4.1 Description of the optimization problem

According to the previous section, the three geometric parameters of the semi-elliptical ribs, rib width (W_r), rib height (H_r), and rib length (L_r), all have noticeable effects on the microchannel performance. The parameter combination in Section 3.5 is selected from limited cases, which may not fully represent the optimal performance of the microchannel across the entire design space. Consequently, it is essential to consider both the thermal and hydraulic performances of the microchannel and optimize these geometric parameters to achieve further performance improvement. With a fixed *Re* number of 440, the two selected objective functions are the heat transfer enhancement factor ($J_1 = -Nu/Nu_0$) and the friction factor ratio ($J_2 = f/f_0$). By introducing a negative sign in J_1, the optimization objective of maximizing heat transfer is transformed into minimize J_1, harmonizing it with the minimization of J_2. This adjustment facilitates the application of optimization algorithms which usually involve minimizing objective functions and streamlines the optimization procedure. The two optimization objectives represent the extent to which the thermal performance and flow resistance of the designed microchannel increase compared to a smooth one. Based on the results of parameter analysis, when W_r, H_r, and L_r are too small, there is no significant enhancement in microchannel performance. Conversely, when they are too large, the increase in flow resistance obviously outweighs the improvement in heat transfer, which is unfavorable for achieving high overall performance. Therefore, the design ranges for W_r, H_r, and L_r are set as [0.10, 0.25 mm], [0.06, 0.18 mm], and [0.4, 0.7 mm], respectively. The optimization problem for the ribbed microchannel can be described as finding the optimal combination of (W_r, H_r, L_r) within the feasible solution range to minimize the objective functions J_1 and J_2 as much as possible, under the operating condition of $Re = 440$.

4.2 Fitting of ANN

Before conducting multi-objective optimization, it is necessary to establish the relationship between the input parameters and output objective functions. Given that relying solely on numerical simulation will require a large number of cases and consume a significant amount of solution time, Artificial Neural Networks (ANNs) [52] are employed and trained as surrogate models to capture the functional relationship between the inputs and outputs. For the dataset, 80 samples are created through numerical simulation. The selected specific values within the design space are as follows: [0.1, 0.15, 0.2, 0.25 mm] for W_r, [0.06, 0.09, 0.12, 0.15, 0.18 mm] for H_r, and [0.4, 0.5, 0.6, 0.7 mm] for L_r. Out of the 80 sets of data, 70% sets are used for training, 15% sets for validation, and 15% sets for testing. Architecture of the employed fully-connected neural network is illustrated in Figure 14, which consists of an input layer, a hidden layer, and an output layer. To achieve nonlinear mapping, the Sigmoid function [52] is used as the activation function. The number of neurons in the hidden layer significantly influences the performance of the ANN model, so it is essential to conduct an independence test on it. During the training process, mean squared error (MSE) and regression coefficient (R^2) are utilized to evaluate the fitting performance of the model. The formulas for *MSE* and R^2 are as follows:

$$\mathrm{MSE} = \frac{1}{N}\sum_{i=1}^{N}(y_i - y_{i,\mathrm{ANN}})^2, \tag{14}$$

$$R^2 = \sqrt{\frac{\sum_{i=1}^{N}(y_{i,\mathrm{ANN}} - \overline{y})^2}{\sum_{i=1}^{N}(y_i - \overline{y})^2}}. \tag{15}$$

Smaller MSE and larger R^2 values indicate better performance of the prediction model. Furthermore, the input is normalized to [0,1], and the Levenberg-Marquardt algorithm [52] is utilized for training.

The independence test results for the number of neurons in the hidden layer are presented in Table 3 below. It is observed that as the number of neurons increases, the MSE on the validation set exhibits an overall trend of initial decrease followed by an increase, while R^2 shows the opposite trend. The reason is that when the number of neurons in the hidden

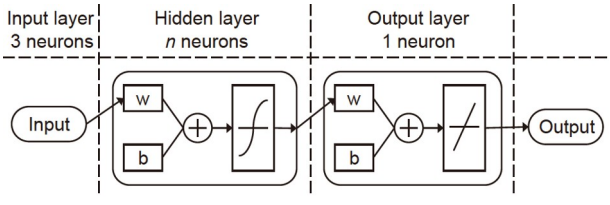

Figure 14 Diagram of the neural network architecture.

Table 3 Independence test on the number of neurons in the hidden layer

Number of neurons in the hidden layer	$J_1 = -Nu/Nu_0$		$J_2 = f/f_0$	
	MSE	R^2	MSE	R^2
1	9.501E-03	0.818	5.443E-04	0.973
2	3.990E-03	0.927	4.114E-04	0.982
3	2.285E-03	0.956	2.625E-04	0.989
4	1.214E-03	0.975	1.454E-04	0.996
5	1.413E-03	0.972	8.605E-05	0.994
6	1.434E-03	0.972	5.740E-05	0.996
7	1.081E-03	0.980	6.169E-05	0.998
8	1.299E-03	0.977	7.693E-05	0.998
9	1.535E-03	0.971	7.559E-05	0.997
10	9.551E-04	0.980	5.017E-05	0.998
11	8.945E-04	0.983	1.116E-04	0.995
12	2.018E-03	0.960	1.071E-04	0.996
13	1.468E-03	0.973	2.343E-04	0.988
14	1.215E-03	0.975	2.765E-04	0.995
15	1.469E-03	0.972	1.213E-04	0.994
16	1.973E-03	0.968	2.233E-04	0.993

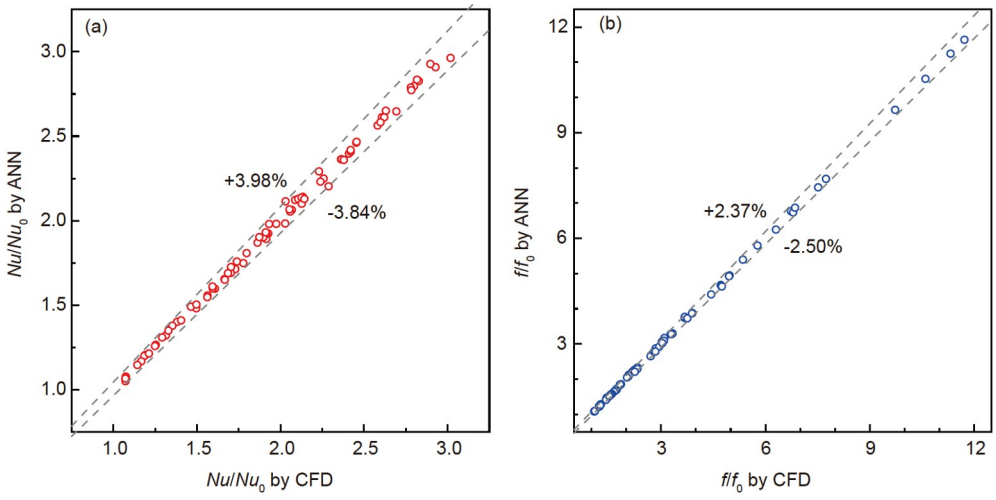

Figure 15 (Color online) Comparison between the CFD and predicted results. (a) Nu/Nu_0; (b) f/f_0.

layer is small, the model's prediction capability is insufficient, indicating underfitting. In this situation, as the number of neurons increases, MSE decreases and R^2 rises. However, when the number of neurons becomes too large, the prediction model, despite its high accuracy on the training set, experiences a noticeable decrease in accuracy on the validation set, indicating overfitting. Based on the test results, the ANN models for objectives J_1 and J_2 are configured with 11 and 10 neurons in the hidden layer, respectively. The comparison between the 80 sets of predicted and simulated results is presented in Figure 15. The upper and lower bounds of prediction error for J_1 are 3.98% and −3.84%, respectively. For J_2, they are 2.37% and −2.50%. The results suggest that the established prediction models are accurate and reliable.

4.3 Optimization results

The NSGA-II [53] is employed for multi-objective optimization in this study. As a heuristic algorithm, it seeks the optimal solution through iteration. The parameter settings for NSGA-II are listed in Table 4. Combined with the well-

Table 4 Parameter settings of NSGA-Ⅱ

Parameter	Value
Population size	200
Pareto fraction	0.3
Generation	50
Crossover fraction	0.8
Migration fraction	0.2
Function tolerance	10^{-5}

trained ANN models, the obtained Pareto front by NSGA-II is presented in Figure 16, containing 60 non-dominated solutions. Compared to dominated solutions, these non-dominated solutions exhibit higher heat transfer at the same flow resistance or lower flow resistance at the same heat transfer performance. Point A in the upper-left corner of the Pareto front represents the solution with the highest thermal performance within the design range. Moving along the Pareto front towards the lower-right side, thermal performance gradually decreases, while hydraulic performance improves until the point B, which represents the solution with the minimum flow resistance. To balance the competing thermal and hydraulic performances, a classical decision-making method, TOPSIS [53], is employed to select an optimal compromise solution from the Pareto front. The core principle of TOPSIS is that the chosen compromise solution should be geometrically closest to the ideal positive solution and furthest from the ideal negative solution. The former refers to the ideal solution that each objective achieves its most satisfactory value, while the latter refers to the ideal solution that each objective achieves its worst value. The two are denoted as points P and N in Figure 16, respectively. The final selected optimal compromise solution is marked as point O, with W_r = 0.2415 mm, H_r = 0.0976 mm, L_r = 0.6486 mm. Accordingly, the microchannel with the optimized ribs has a heat transfer enhancement factor of Nu/Nu_0 = 2.499, a friction factor ratio of f/f_0 = 3.155, and a PEC value of 1.704, exhibiting excellent overall performance. To validate the optimization results, numerical simulation is conducted on the optimized microchannel at Re = 440. The numerical results reveal that the optimized microchannel has Nu/Nu_0 = 2.559, f/f_0 = 3.316, and PEC = 1.716. The relatively errors of the predicted results for the three performances are 2.32%, 4.84%, and 0.69%, respectively. This demonstrates the reliability of the optimization results.

The optimization is conducted under the fixed condition of Re = 440, while flow condition is usually variable in practice. Therefore, performance testing on the optimized microchannel obtained at Re = 440 is extended to a wider Re range of 220–660. In order to intuitively show its thermal-hydraulic performance, Figure 17 presents a comparison of Nu, f, and PEC between the CFD-simulated microchannels in Section 3 and the intelligently optimized microchannel.

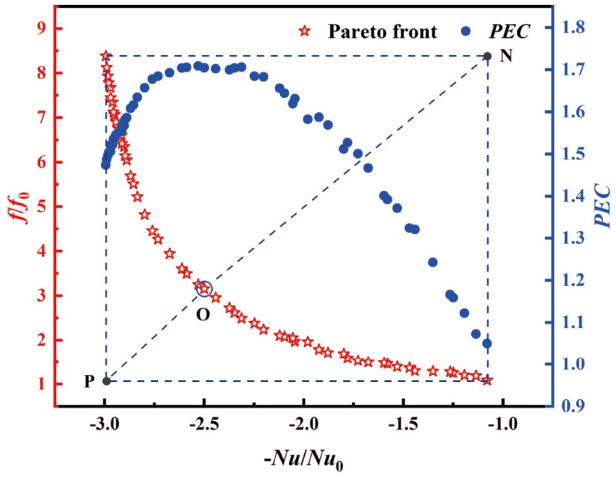

Figure 16 (Color online) The obtained Pareto front and optimal comprise solution.

Within the data shown in Figure 17, it is evident that the optimized microchannel showcases high heat transfer and middle flow resistance, thus achieving excellent overall performance. Notably, except for the flow condition of Re = 220 where the PEC of the optimized microchannel is close to the highest, it achieves the highest PEC values at other four flow conditions. Therefore, the optimized microchannel not only achieves superior performance under the flow condition for multi-objective optimization, but also demonstrates excellent performance across various flow conditions. The Nu, f, and PEC of the optimized microchannel fall in 12.63–21.96, 0.081–0.114, and 1.572–1.723, respectively. The performance testing verifies the excellent performance of the optimized microchannel and the effectiveness of multi-objective optimization.

5 Conclusions

In this study, numerical simulations are conducted to compare the flow characteristics of the designed microchannel with semi-elliptical ribs to those of a smooth microchannel. The effects of three geometrical parameters, rib width (W_r), rib height (H_r), and rib length (L_r), on the thermal and hydraulic performances of the microchannel are analyzed within the Re range of 220–660. To further improve the microchannel performance, a multi-objective optimization on the ribs is performed using the ANN-based surrogate models in conjunction with NSGA-II. Subsequently, an optimal compromise solution is determined from the Pareto front using the TOPSIS method, and performance testing on the optimized microchannel is carried out. The main conclusions can be drawn as follows.

Periodically arranged staggered semi-elliptical ribs induce periodic vortices within the microchannel. Increasing W_r leads to more pronounced vortex flow and enhanced fluid

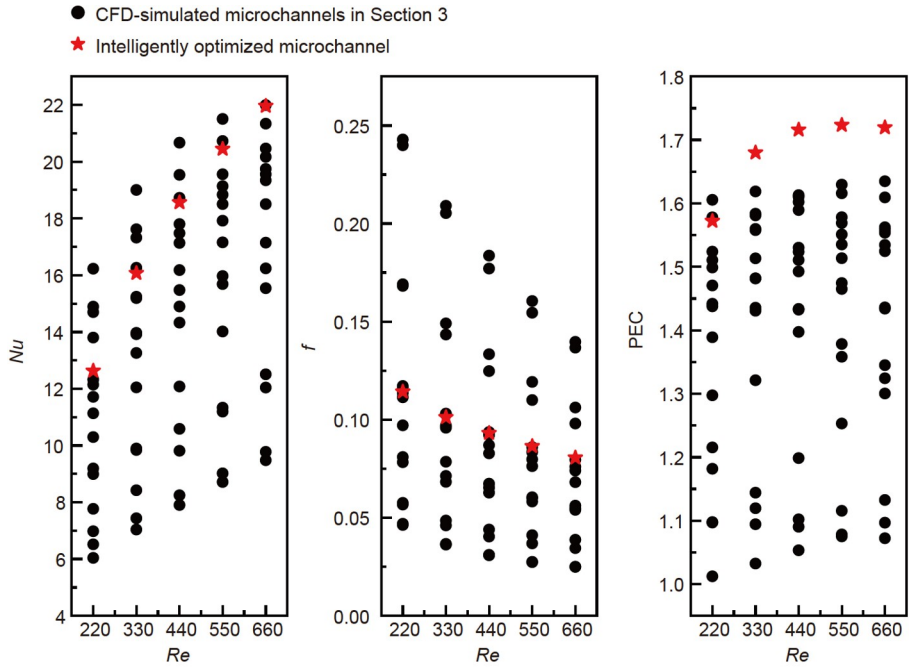

Figure 17 Comparison of *Nu*, *f*, and PEC between the CFD-simulated microchannels in Section 3 and the intelligently optimized microchannel.

mixing. However, as H_r and L_r increase, the characteristics of vortices become initially more significant while then diminishing. Furthermore, the ribs intensify the local jet effect and generate disturbances to the fluid, resulting in the thinning of the thermal boundary layer. Consequently, heat transfer in the microchannel is significantly enhanced.

Both the Nusselt number (*Nu*) and fanning friction factor (*f*) of the microchannel increase with rising W_r and H_r. However, they exhibit a trend of initial growth followed by a decline as L_r increases. The PEC initially increases and then decreases as all three rib parameters increase. The influence of L_r on the thermal and hydraulic performances of the microchannel is comparatively weaker than that of W_r and H_r, but they have a similar impact on the overall performance. Within a specific range, increasing L_r enhances heat transfer without causing significant deterioration in hydraulic performance.

Among the numerically examined configurations, the microchannel with W_r = 0.20 mm, H_r = 0.12 mm, and L_r = 0.5 mm demonstrates excellent overall performance, showing minor variations across different *Re* numbers. The *Nu* ranges from 12.32 to 19.56, *f* ranges from 0.076 to 0.116, and PEC ranges from 1.524 to 1.589.

At *Re* = 440, the Pareto front considering both heat transfer enhancement and flow resistance is obtained, and the selected optimal compromise solution is W_r = 0.2415 mm, H_r = 0.0976 mm, and L_r = 0.6486 mm. Performance testing shows that the optimized ribbed microchannel exhibits high heat transfer and middle flow resistance, thus achieving excellent overall performance. Within the *Re* range of 220–660, the PEC ranges from 1.572 to 1.723. Overall, this paper presents a ribbed microchannel design capable of achieving excellent overall performance across wide laminar flow conditions.

This work was supported by the National Natural Science Foundation of China (Grant No. 52076088) and the National Key Research and Development Program of China (Grant No. 2022YFB4003801).

1 He Z, Yan Y, Zhang Z. Thermal management and temperature uniformity enhancement of electronic devices by micro heat sinks: A review. Energy, 2021, 216: 119223
2 Sadique H, Murtaza Q, Samsher Q. Heat transfer augmentation in microchannel heat sink using secondary flows: A review. Int J Heat Mass Transfer, 2022, 194: 123063
3 Du L, Hu W. An overview of heat transfer enhancement methods in microchannel heat sinks. Chem Eng Sci, 2023, 280: 119081
4 Li S, Zhang H, Cheng J, et al. A state-of-the-art overview on the developing trend of heat transfer enhancement by single-phase flow at micro scale. Int J Heat Mass Transfer, 2019, 143: 118476
5 Yan Z, Huang X, Yang C. Hydrodynamic effects on particle deposition in microchannel flows at elevated temperatures. J Heat Transfer, 2018, 140: 012402
6 Tuckerman D B, Pease R F W. High-performance heat sinking for VLSI. IEEE Electron Device Lett, 1981, 2: 126–129
7 Hu D H, Zhang Z W, Li Q. Numerical study on flow and heat transfer characteristics of microchannel designed using topological optimizations method. Sci China Tech Sci, 2019, 63: 105–115
8 Rimbault B, Nguyen C T, Galanis N. Experimental investigation of CuO–water nanofluid flow and heat transfer inside a microchannel heat sink. Int J Therm Sci, 2014, 84: 275–292
9 Mohammed H A, Gunnasegaran P, Shuaib N H. Influence of channel shape on the thermal and hydraulic performance of microchannel heat sink. Int Commun Heat Mass Transfer, 2011, 38: 474–480
10 Wen Z X, Lv Y G, Li Q. Comparative study on flow and heat transfer characteristics of sinusoidal and zigzag channel printed circuit heat exchangers. Sci China Tech Sci, 2020, 63: 655–667
11 Ansari M Q, Zhou G. Flow and heat transfer analysis of microchannels structured with rectangular surface roughness. Chem Eng Processing-Process Intensification, 2020, 156: 108066
12 Hong F, Cheng P. Three dimensional numerical analyses and opti-

mization of offset strip-fin microchannel heat sinks. Int Commun Heat Mass Transfer, 2009, 36: 651–656
13 Kuppusamy N R, Mohammed H A, Lim C W. Thermal and hydraulic characteristics of nanofluid in a triangular grooved microchannel heat sink (TGMCHS). Appl Math Computation, 2014, 246: 168–183
14 Xia G D, Zhai Y L, Cui Z Z. Characteristics of entropy generation and heat transfer in a microchannel with fan-shaped reentrant cavities and internal ribs. Sci China Tech Sci, 2013, 56: 1629–1635
15 Lan Y, Feng Z, Huang K, et al. Effects of truncated and offset pin-fins on hydrothermal performance and entropy generation in a rectangular microchannel heat sink with variable fluid properties. Int Commun Heat Mass Transfer, 2021, 124: 105258
16 Chai L, Xia G D, Wang H S. Parametric study on thermal and hydraulic characteristics of laminar flow in microchannel heat sink with fan-shaped ribs on sidewalls—Part 1: Heat transfer. Int J Heat Mass Transfer, 2016, 97: 1069–1080
17 Chai L, Xia G D, Wang H S. Parametric study on thermal and hydraulic characteristics of laminar flow in microchannel heat sink with fan-shaped ribs on sidewalls—Part 2: Pressure drop. Int J Heat Mass Transfer, 2016, 97: 1081–1090
18 Chai L, Xia G D, Wang H S. Parametric study on thermal and hydraulic characteristics of laminar flow in microchannel heat sink with fan-shaped ribs on sidewalls—Part 3: Performance evaluation. Int J Heat Mass Transfer, 2016, 97: 1091–1101
19 Di Capua H M, Escobar R, Diaz A J, et al. Enhancement of the cooling capability of a high concentration photovoltaic system using microchannels with forward triangular ribs on sidewalls. Appl Energy, 2018, 226: 160–180
20 Pan M, Wang H, Zhong Y, et al. Experimental investigation of the heat transfer performance of microchannel heat exchangers with fan-shaped cavities. Int J Heat Mass Transfer, 2019, 134: 1199–1208
21 Khan M, Shuja S Z, Yilbas B S, et al. A case study on innovative design and assessment of a microchannel heat sink with various turbulators arrangements. Case Studies Therm Eng, 2022, 31: 101816
22 Lori M S, Vafai K. Heat transfer and fluid flow analysis of microchannel heat sinks with periodic vertical porous ribs. Appl Therm Eng, 2022, 205: 118059
23 Wang G, Chen T, Tian M, et al. Fluid and heat transfer characteristics of microchannel heat sink with truncated rib on sidewall. Int J Heat Mass Transfer, 2020, 148: 119142
24 Li P, Luo Y, Zhang D, et al. Flow and heat transfer characteristics and optimization study on the water-cooled microchannel heat sinks with dimple and pin-fin. Int J Heat Mass Transfer, 2018, 119: 152–162
25 Wang X Y, Xu X H, Liang X G. Enhancement of laminar flow heat transfer with single/double-inclined ribs for unilaterally-heated channel. Sci China Tech Sci, 2023, 66: 2108–2118
26 Fiebig M. Embedded vortices in internal flow: Heat transfer and pressure loss enhancement. Int J Heat Fluid Flow, 1995, 16: 376–388
27 Awais M, Bhuiyan A A. Heat transfer enhancement using different types of vortex generators (VGs): A review on experimental and numerical activities. Therm Sci Eng Prog, 2018, 5: 524–545
28 Wang Y, Zhou B, Liu Z, et al. Numerical study and performance analyses of the mini-channel with discrete double-inclined ribs. Int J Heat Mass Transfer, 2014, 78: 498–505
29 Chen C, Teng J T, Cheng C H, et al. A study on fluid flow and heat transfer in rectangular microchannels with various longitudinal vortex generators. Int J Heat Mass Transfer, 2014, 69: 203–214
30 Ebrahimi A, Roohi E, Kheradmand S. Numerical study of liquid flow and heat transfer in rectangular microchannel with longitudinal vortex generators. Appl Therm Eng, 2015, 78: 576–583
31 Zhang J F, Jia L, Yang W W, et al. Numerical analysis and parametric optimization on flow and heat transfer of a microchannel with longitudinal vortex generators. Int J Therm Sci, 2019, 141: 211–221
32 Gönül A, Okbaz A, Kayaci N, et al. Flow optimization in a microchannel with vortex generators using genetic algorithm. Appl Therm Eng, 2022, 201: 117738
33 Cheng J C, Tsay Y L, Liu C T, et al. Heat transfer enhancement of microchannel heat sink with longitudinal vortex generators and bypass jet flow. Numer Heat Transfer Part A-Appl, 2020, 77: 807–819
34 Zheng S, Feng Z, Lin Q, et al. Numerical investigation on thermal–hydraulic characteristics in a mini-channel with trapezoidal cross-section longitudinal vortex generators. Appl Therm Eng, 2022, 205: 118004
35 Feng Z, Jiang P, Zheng S, et al. Experimental and numerical investigations on the effects of insertion-type longitudinal vortex generators on flow and heat transfer characteristics in square minichannels. Energy, 2023, 278: 127855
36 Feng Z, Zhou C, Guo F, et al. The effects of staggered triangular ribs induced vortex flow on hydrothermal behavior and entropy generation in microchannel heat sink. Int J Therm Sci, 2023, 191: 108331
37 Al-Asadi M T, Alkasmoul F S, Wilson M C T. Heat transfer enhancement in a micro-channel cooling system using cylindrical vortex generators. Int Commun Heat Mass Transfer, 2016, 74: 40–47
38 Kumar Das A, Hiremath S S. Experimental and numerical analysis of thermohydraulic performance and entropy-generation in a rectangular microchannel for laminar and single-phase flow: Parametric study and multi-objective optimization. Therm Sci Eng Prog, 2022, 33: 101375
39 Ge Y, Liu Z, Shan F, et al. Multi-objective arrangement optimization of a tube bundle in cross-flow using CFD and genetic algorithm. Energy Procedia, 2017, 142: 3774–3779
40 Shi C Y, Yu M J, Liu W, et al. Shape optimization of corrugated tube using B-spline curve for convective heat transfer enhancement based on machine learning. Sci China Tech Sci, 2022, 65: 2734–2750
41 Zheng Z J, Xu Y, He Y L. Thermal analysis of a solar parabolic trough receiver tube with porous insert optimized by coupling genetic algorithm and CFD. Sci China Tech Sci, 2016, 59: 1475–1485
42 Yang Y T, Tang H W, Ding W P. Optimization design of microchannel heat sink using nanofluid by numerical simulation coupled with genetic algorithm. Int Commun Heat Mass Transfer, 2016, 72: 29–38
43 Husain A, Kim K Y. Enhanced multi-objective optimization of a microchannel heat sink through evolutionary algorithm coupled with multiple surrogate models. Appl Therm Eng, 2010, 30: 1683–1691
44 Sikirica A, Grbčić L, Kranjčević L. Machine learning based surrogate models for microchannel heat sink optimization. Appl Therm Eng, 2023, 222: 119917
45 Das A K, Hiremath S S. Multi-objective optimization of a novel butterfly-wing vortex generator fabricated in a rectangular microchannel based on CFD and NSGA-II genetic algorithm. Appl Therm Eng, 2023, 234: 121187
46 Wang G, Ding G, Liu R, et al. Multi-objective optimization of a bidirectional-ribbed microchannel based on CFD and NSGA-II genetic algorithm. Int J Therm Sci, 2022, 181: 107731
47 Xiao H, Liu Z, Liu W. Conjugate heat transfer enhancement in the mini-channel heat sink by realizing the optimized flow pattern. Appl Therm Eng, 2021, 182: 116131
48 Chai L, Xia G, Wang L, et al. Heat transfer enhancement in microchannel heat sinks with periodic expansion–constriction cross-sections. Int J Heat Mass Transfer, 2013, 62: 741–751
49 Chai L, Xia G D, Wang H S. Numerical study of laminar flow and heat transfer in microchannel heat sink with offset ribs on sidewalls. Appl Therm Eng, 2016, 92: 32–41
50 Zhu Q, Xia H, Chen J, et al. Fluid flow and heat transfer characteristics of microchannel heat sinks with different groove shapes. Int J Therm Sci, 2021, 161: 106721
51 Sudheer A P, Madanan U. Numerical investigation into heat transfer augmentation in a square minichannel heat sink using butterfly inserts. Therm Sci Eng Prog, 2022, 36: 101522
52 Biswas M A R, Robinson M D, Fumo N. Prediction of residential building energy consumption: A neural network approach. Energy, 2016, 117: 84–92
53 Ge Y, Liu Z, Liu W. Multi-objective genetic optimization of the heat transfer for tube inserted with porous media. Int J Heat Mass Transfer, 2016, 101: 981–987